Journal of Solid State Chemistry 262 (2018) 142–148

Contents lists available at ScienceDirect

Journal of Solid State Chemistry

journal homepage: www.elsevier.com/locate/jssc

Structural properties of barium stannate

D. Phelan[a,*], F. Han[b,c], A. Lopez-Bezanilla[a], M.J. Krogstad[a,d], Y. Gim[e], Y. Rong[a], Junjie Zhang[a], D. Parshall[f], H. Zheng[a], S.L. Cooper[e], M. Feygenson[g,h], Wenge Yang[b,c], Yu-Sheng Chen[i]

[a] Materials Science Division, Argonne National Laboratory, Lemont, IL 60439, USA
[b] High Pressure Synergetic Consortium, Geophysical Laboratory, Carnegie Institute of Washington, Argonne, IL 60439, USA
[c] Center for High Pressure Science and Technology Advanced Research, Shanghai 201203, China
[d] Physics Department, Northern Illinois University, DeKalb, IL 60115, USA
[e] Department of Physics and Frederick Seitz Materials Research Laboratory, University of Illinois, Urbana, IL 61801, USA
[f] National Institute of Standards and Technology, NIST Center for Neutron Research, Gaithersburg, MD 20899, USA
[g] Chemical and Engineering Materials Division, Neutron Sciences Directorate, Oak Ridge National Laboratory, Oak Ridge, TN 37830, USA
[h] Jülich Centre for Neutron Science, Forschungszentrum Jülich, Jülich 52428, Germany
[i] ChemMatCARS, The University of Chicago, Argonne, IL 60439, USA

ARTICLE INFO

Keywords:
Structure
Diffraction
Oxides
Semiconductor

ABSTRACT

$BaSnO_3$ has attracted attention as a transparent conducting oxide with high room temperature carrier mobility. We report a series of measurements that were carried out to assess the structure of $BaSnO_3$ over a variety of length scales. Measurements included single crystal neutron and x-ray diffraction, Rietveld and pair distribution analysis of neutron powder diffraction, Raman scattering, and high-pressure x-ray diffraction. Results from the various diffraction probes indicate that both the long-range and local structures are consistent with the cubic symmetry. The diffraction data under pressure was consistent with a robustly cubic phase up to 48.9 GPa, which is supported by density functional calculations. Additionally, transverse phonon velocities were determined from measured dispersion of the transverse acoustic phonon branches, the results of which are in good agreement with previous theoretical estimates and ultrasound measurements.

1. Introduction

Barium Stannate, $BaSnO_3$, is a wide bandgap semiconductor (experimental values of the gap vary from 2.95 to 4.05 eV [1–6]) that has attracted considerable recent interest, because when doped, $BaSnO_3$ possesses large carrier mobilities (μ) for n-type conduction at room temperature at relatively high carrier densities (n); for example, $\mu \leq 320\,cm^2V^{-1}s^{-1}$ at $n \sim 8 \times 10^{19}\,cm^{-3}$ [5–7]. Transparent conducting behavior has been demonstrated in various single crystals and epitaxial films through either rare earth (e.g., La^{3+} [5–9]) substitution on the A-site or via oxygen vacancies [6,10,11]. Density functional theory (DFT) calculations indicate that the lower conduction band consists of hybridized s and p-states of Sn and O atoms, which leads to a low electron effective mass [12]. The low effective mass of the charge carriers combined with the shallow donor level for La^{3+} in $BaSnO_3$ leads to the transparent conducting behavior [12].

Interestingly, although the structure of $BaSnO_3$ has been continually described in terms of the cubic perovskite structure (space group *Pm-3 m*), some DFT calculations have suggested that there are phonon instabilities on the zone boundaries [12]. Liu *et al.* obtained imaginary phonon frequencies at both the M (½, ½, 0) and R (½, ½, ½) points of the cubic Brillouin zone. For perovskites, these instabilities often arise due to rotations of oxygen octahedra that allow the structure to adapt to a mismatch in (A+O) radii to (B+O) radii. Such distortions lead to a lowering of the symmetry and a larger unit cell that incorporates more than one formula unit [13]. Commonly, the resulting space group is orthorhombic (*Pnma* or equivalently *Pbnm*) or rhombohedral (*R-3c*). In contrast, the phonon calculations of Stanislavchuk *et al.* showed no unstable modes on the zone boundaries [14], although their calculations yielded very similar formation energies for the cubic, orthorhombic, and rhombohedral structures. Moreover, they reported the presence of Raman peaks, which are forbidden as first-order scattering cross-sections for cubic symmetry. Based on this result, Stanislavchuk *et al.* suggested that $BaSnO_3$ may exhibit local orthorhombic lattice distortions [14]. The occurrence of oxygen tilt instabilities or local lattice distortions may have implications on the carrier mobility in $BaSnO_3$; for example, a soft optical phonon mode associated with a cubic-orthorhombic/rhombohedral distortion may induce electron-phonon scattering events, and local static structural distortions may serve as a source of electron scattering.

* Corresponding author.
E-mail address: dphelan@anl.gov (D. Phelan).

https://doi.org/10.1016/j.jssc.2018.01.019
Received 1 December 2017; Received in revised form 18 January 2018; Accepted 21 January 2018
Available online 31 January 2018

It is therefore important to consider these possibilities as they could have implications on engineering compounds with higher mobilities.

We report the results of a variety of scattering experiments that were performed to assess whether $BaSnO_3$ possesses structural deviations from cubic symmetry on either long-range or short-range length scales. Rietveld refinements of powder neutron diffraction data are consistent with an average cubic structure between 100 K and 500 K. Pair density function analysis similarly is well-described by the cubic structure and shows no evidence of long-range or local structural distortions. Single crystal neutron diffraction and synchrotron x-ray diffraction measurements reveal neither sharp nor diffuse Bragg peaks at the M or R points, again providing no evidence of either local or long-range static lattice distortions. Raman measurements performed on single crystals suggest a likely defect-induced mode at 140 cm^{-1} and a mode of uncertain origin at 247 cm^{-1}, but reveal neither of the strong first-order modes at ~ 408 cm^{-1} or 724 cm^{-1} which had been previously attributed to optical modes at the M-points allowed by local orthorhombic distortions [14]. High pressure x-ray diffraction measurements and calculations suggest that the cubic phase is stable to the highest measured pressure (~ 49 GPa). Furthermore, we have measured the transverse phonon velocity via inelastic neutron scattering along both the [110] and [100] directions.

2. Materials and methods

Polycrystalline $BaSnO_3$ was grown by standard solid-state reaction using $BaCO_3$ and SnO_2 as starting materials. Single crystals of $BaSnO_{3-\delta}$ were grown from Cu_2O flux using the method described by Kim *et al.* [10]. Consistent with previous reports, the single crystals showed n-type conductivity that most likely arises due to a low concentration of oxygen vacancies [6,8,10]. Crystals with masses of 30–70 mg were employed in the neutron scattering measurements.

Time-of-flight powder neutron diffraction measurements were performed on the beamline NOMAD located at the Spallation Neutron Source (SNS) at Oak Ridge National Laboratory [15]. The sample was measured in a thin-walled quartz tube in a Cobra cryostream at various temperatures between 100 K and 500 K. Rietveld refinement was carried out using GSAS [16] with EXPGUI [17] interface for a d-spacing range from $0.420 < d < 1.505$ Å. The structure function $S(|\boldsymbol{Q}|)$ was obtained by subtracting the background of the empty capillary and normalizing the data to the scattering from a solid vanadium rod. Pair distribution function (pdf) refinement was carried out using PDFgui/PDFfit2 [18], and termination ripples were simulated in the fit. Single crystal x-ray diffraction measurements were performed on 15-ID-B at the Advanced Photon Source (APS) at Argonne National Laboratory using $\lambda = 0.413280$ Å and an APEX II CCD detector. Elastic single crystal neutron scattering measurements were performed on the thermal triple-axis spectrometer, BT-7, located at the NIST Center for Neutron Research. The scan through the R-point discussed later in the paper (Fig. 4a) was performed on one single crystal aligned in the cubic (hhl) scattering plane. The other scans were performed on 3 co-aligned crystals aligned in the cubic ($hk0$) scattering plane. A fixed final neutron energy of $E_f = 14.7$ meV was employed, and beam harmonics were suppressed through use of pyrolytic graphite filters. Inelastic neutron scattering measurements were also performed on BT-7 using the 3 co-aligned crystals. The angle-dispersive XRD experiments under high pressure were performed at the HPCAT beamline 16-BM-D at the Advanced Photon Source, Argonne National Laboratory. A MAR345 image plate detector was equipped in the beamline and the diffraction was processed in transmission mode. The wavelength of X-ray for the experiments was set to 0.4246 Å. The application of high pressure was realized with a pair of 300 μm-cutlet diamonds mounted on a symmetric diamond anvil cell. A 301 stainless steel sheet was used as a gasket, and Neon was loaded into the gasket as a pressure-transmitting medium.

Temperature-dependent Raman scattering measurements were performed using the 647.1 nm excitation line from a Kr^+ laser and room temperature measurements were performed using a Nanophoton Raman microscope with a 532 nm laser. The 647.1 nm Raman system's incident laser power was limited to 5 mW, and was focused to a ~50 μm-diameter spot to minimize laser heating of the sample. The scattered light from the samples was collected in a backscattering geometry, dispersed through a triple-stage spectrometer, and then detected with a liquid-nitrogen-cooled CCD detector. The incident light polarization was controlled using a polarization rotator, and the scattered light polarization was analyzed with a linear polarizer, allowing the determination of excitation symmetry information. For the temperature-dependent measurements, the sample was inserted into a continuous He-flow cryostat, which allowed the sample temperature to be varied between 3 and 300 K.

The measurements using the Nanophoton Raman Microscope system were performed using a 532 nm excitation line with an imaging spatial resolution of 350 nm × 800 nm. The incident laser power was limited to 0.5 mW to minimize laser heating. The scattered light from the sample was collected in a backscattering geometry, through a confocal slit, dispersed through a triple-stage spectrometer and then detected with electrically cooled CCD detector cooled to −70 °C. For the room temperature measurement, the sample was kept on a microscope slide.

3. Results

3.1. Powder neutron diffraction

An example of a powder neutron diffraction pattern (100 K) and its Rietveld refinement is displayed in Fig. 1. Consistent with previous reports, all peaks in the pattern are described by cubic symmetry, with no unexpected splitting of fundamental peaks observed at any measured temperature (100 – 500 K). Furthermore, no superlattice peaks at either the M or R points were observed at any temperature. The obtained lattice parameters, thermal displacement parameters, and agreement factors at various temperatures are provided in Table 1.

Although the Rietveld refinements were consistent with an average cubic structure, they do not preclude the possibility of local distortions. We have therefore investigated the same data using pdf analysis which is a measure of the local structure that has been shown to be quite different than the average structure in a number of perovskites [19]. The pdf analysis is made possible by the time-of-flight diffraction in which data is collected up to large wave-vector transfers ($|\boldsymbol{Q}|$) and Fourier transformed from reciprocal space up to $|\boldsymbol{Q}| = 31.4$ Å^{-1} to obtain a high-resolution pdf in real space. Essentially, the Fourier transform is performed on the measured structure function, $S(|\boldsymbol{Q}|)$, which yields a pair correlation function, G(r), defined by [20]:

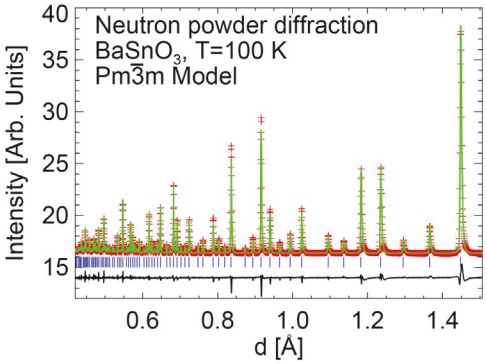

Fig. 1. Rietveld refinement of powder neutron diffraction data for $BaSnO_3$ at 100 K. Data points are shown by red + symbols and the fit is shown in solid red. Short blue lines mark the positions of Bragg reflections, and the difference curve is shown in solid black. (For interpretation of the references to color in this figure legend, the reader is referred to the web version of this article.)

Table 1
Results of Rietveld refinement of powder neutron diffraction data. The thermal parameters shown are isotropic. The value of the 300 K lattice parameter is lower than the accepted value [5–7], which may indicate the lattice parameters are systematically low.

T [K]	a [Å]	U_{Ba} [Å^2]	U_{Sn} [Å^2]	U_O [Å^2]	$R(F^2)$ [%]
100	4.095703(44)	0.00008(11)	−0.00034(10)	0.00266(7)	6.8
125	4.096139(48)	0.00047(12)	−0.00009(11)	0.00304(8)	4.6
150	4.096614(48)	0.00079(12)	0.00005(11)	0.00333(8)	4.7
175	4.097172(48)	0.00113(13)	0.00015(11)	0.00364(8)	4.9
200	4.097729(49)	0.00145(13)	0.00029(11)	0.00403(8)	5.1
225	4.098405(49)	0.00182(13)	0.00042(11)	0.00437(8)	5.1
250	4.099096(49)	0.00209(13)	0.00053(11)	0.00473(9)	5.5
275	4.099791(49)	0.00245(13)	0.00064(11)	0.00510(9)	5.7
300	4.100489(49)	0.00272(13)	0.00078(11)	0.00545(9)	5.6
325	4.101280(51)	0.00314(14)	0.00093(11)	0.00588(9)	5.8
350	4.102056(48)	0.00335(14)	0.00099(11)	0.00622(9)	6.1
375	4.102853(51)	0.00368(14)	0.00111(11)	0.00659(10)	6.3
400	4.103526(49)	0.00394(14)	0.00120(11)	0.00690(9)	6.3
425	4.104308(51)	0.00429(15)	0.00133(12)	0.00730(10)	7.3
450	4.104957(49)	0.00450(14)	0.00139(11)	0.00755(10)	8.0
500	4.106390(49)	0.00491(15)	0.00154(11)	0.00813(10)	8.4

$$G(r) = \frac{2}{\pi}\int_0^\infty |\boldsymbol{Q}|[S(|\boldsymbol{Q}|)-1]\sin(|\boldsymbol{Q}|r)d|\boldsymbol{Q}|$$

The peaks in G(r) describe the distribution of bond-lengths in the sample. G(r) for the data at 100 K is shown in Fig. 2. G(r) was then refined using the program PDFGUI [18] assuming the cubic structure, and it was found that an excellent agreement between the local structure and the cubic model was obtained. Thus, the powder neutron diffraction measurements for $BaSnO_3$ were consistent with a simple cubic perovskite structure on both average and local length scales.

3.2. Single crystal x-ray diffraction

Single crystals provide a means to test for weak Bragg reflections that would be expected to appear on the zone boundaries due to a lowering of the symmetry. Fig. 3(a) and (b) show schematics of the allowed reflections in the pseudocubic (a~4.1 Å) (hk0) and (hk½) planes for a twinned crystal with the rhombohedral $R\bar{3}c$ space group, while Fig. 3(c) and (d) show the same planes for a twinned crystal with the *Pnma* space group. The $R\bar{3}c$ space group produces additional peaks on certain R points of the cubic Brillouin zone, whereas the *Pnma* space group produces additional peaks on certain X (½, 0, 0), M, and R points. The measured pseudocubic (*hk*0) and (*hk*½) scattering planes are shown in Fig. 3(e) and (f), respectively; these reveal no additional Bragg peaks or diffuse peaks, and are thus completely consistent with cubic symmetry.

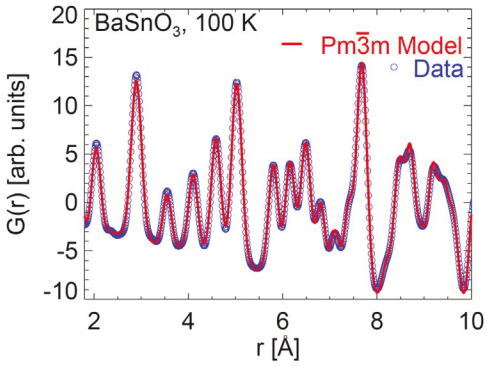

Fig. 2. Real space refinement of G(r) using the $Pm\bar{3}m$ space group. Data are shown by unfilled blue circles, while the fit is shown by the continuous red line. Fourier oscillations were included in the fit to account for noise in the data at low r. (For interpretation of the references to color in this figure legend, the reader is referred to the web version of this article.)

3.3. Single crystal neutron diffraction

Single crystal neutron diffraction was also employed to investigate the possibility of weak reflections at zone boundaries because of its relatively high sensitivity to oxygen displacements compared to x-rays. Fig. 4(a) shows an elastic neutron scan measured through the R-point of a single crystal at 16 K with the crystal aligned in the (hhl) scattering plane. No Bragg peak, sharp or diffuse, was observed, indicating that the structure is not rhombohedral. Fig. 4(b) shows an elastic neutron scan measured through the M-point using three crystals co-aligned in the (hk0) scattering plane at 200 K. Again, the absence of a peak is consistent with the cubic symmetry.

3.4. Raman scattering

A cubic perovskite has no first-order Raman active modes; therefore, distortions in either the average or local structure can be evidenced by the observation of forbidden modes. Raman scattering measurements were performed on two $BaSnO_{3-\delta}$ crystals, and qualitatively similar results were obtained for both crystals at 300 K, one of which is shown in Fig. 5. We note that the crystals showed peaks at the same energies regardless of the spot position on the crystal, demonstrating sample homoegeneity, and that different scattering polarizations were used to make sure that all Raman active peaks were measured. The most prominent feature in the spectra is a sharp mode at $\hbar\omega$ ~ 140 cm^{-1}. The narrowness of this mode suggests that it is likely defect-induced with very few relaxation channels; moreover, additional measurements performed down to 4 K demonstrated very little temperature dependence, consistent with a defect-induced mode. Nevertheless, we note that the nature of this defect remains unclarified. Less prominent, broader features were observed at $\hbar\omega$ ~ 247, 376, 614, and 836 cm^{-1}. Although ultimately the precise origin of these peaks is unknown, a possible origin could be two-phonon scattering from the cubic lattice. Prominent modes previously reported [14] at 724 and 408 cm^{-1} were not observed in the present measurements.

3.5. Stability of the cubic phase under pressure

Though the measurements presented above strongly suggest that $BaSnO_3$ is cubic at room temperature, if it lies near a structural instability, then the low symmetry phase might become stable under pressure. For example, the tetragonal phase is stabilized in (isostructural) $SrTiO_3$ under applied pressure [21]. We have therefore carried out high pressure x-ray synchrotron diffraction experiments at room temperature to determine the pressure dependence of the structure. Fig. 6(a) shows powder x-ray diffraction measurements made under various pressures up to ~ 49 GPa. No splitting of Bragg reflections was resolved under applied pressure, suggesting robust stability of the cubic state, though we note that broadening due to strain was observed upon increasing pressure which could mask a subtle structural distortion. The cubic lattice parameter was extracted as a function of pressure using the program DICVOL 06 from the positions of at least six unique peaks, and their pressure dependence is shown in Fig. 6(b). The pressure-dependent lattice constant was used to fit to the 3rd order Birch-Murnaghan equation [22,23]:

$$P = \frac{3}{2}B_0[(V_0/V)^{7/3} - (V_0/V)^{5/3}]\left\{1+\frac{3}{4}(B_0' - 4)[(V_0/V)^{2/3}-1]\right\}$$

to extract the bulk modulus, B_0, and its pressure derivative B_0', and volume under zero pressure V_0. The resultant fit yielded B_0 = 176 GPa, B_0' = 5.4, V_0 = 69.62 Å^3, and is in good agreement with the data as shown by the solid curve in Fig. 6(b). Estimates of the bulk modulus in

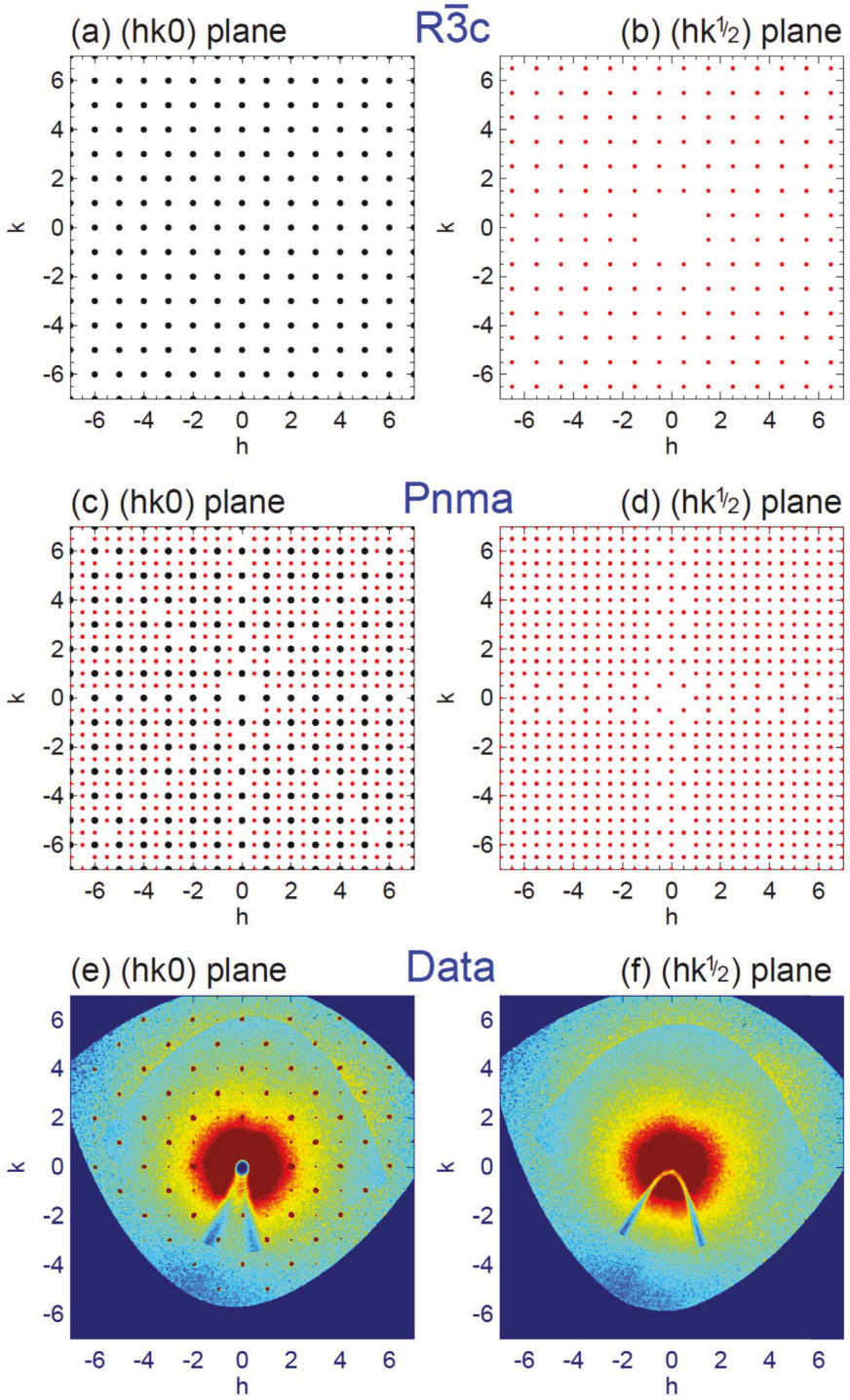

Fig. 3. Single crystal x-ray diffraction for $BaSnO_3$ at 200 K. (a) and (b) show schematics of the (hk0) pseudocubic (a ~ 4.1 Å) scattering plane for the $R\bar{3}c$ and *Pnma* space groups, respectively, and the corresponding measurement is shown in (c). (d) and (e) similarly show schematics of the (hk½) pseudocubic scattering plane for the *R*-3c and *Pnma* space groups, respectively, and the corresponding measurement is shown in (f). In the schematics, the larger (black) symbols indicate peaks for which h, k, and l are all integers and thus allowed by $Pm\bar{3}m$. The smaller (red) symbols indicate peaks for which at least one of h, k, or l is non-integer and are thus forbidden by $Pm\bar{3}m$ symmetry. (For interpretation of the references to color in this figure legend, the reader is referred to the web version of this article.)

the literature include 178 GPa from x-ray measurements taken up to 15 GPa [24], 146 GPa from measurements of sound velocities [25], 182 GPa from LDA calculations [26], and 144 GPa from GGA calculations [26].

Density functional theory calculations were also performed to assess the stability of the cubic phase under pressure. The hybrid functional HSE03 [27] as implemented in the VASP code [28] was used to compute the electronic structure of the material and phonon dispersion curves [29] at both ambient and high (P~50 Gpa) pressure in cubic structures with lattice parameters of 4.155 and 3.880 Å respectively, as shown in Fig. 7(a) and (b). The general shapes of the dispersion curves are consistent with one another, the main difference being the shift to higher frequencies under high pressure. Importantly, the calculated mode frequencies are both real and non-zero at the M, R and X points at both pressures, consistent with a cubic structure. Bouhemadou et al. [26] have previously studied the stability criteria of

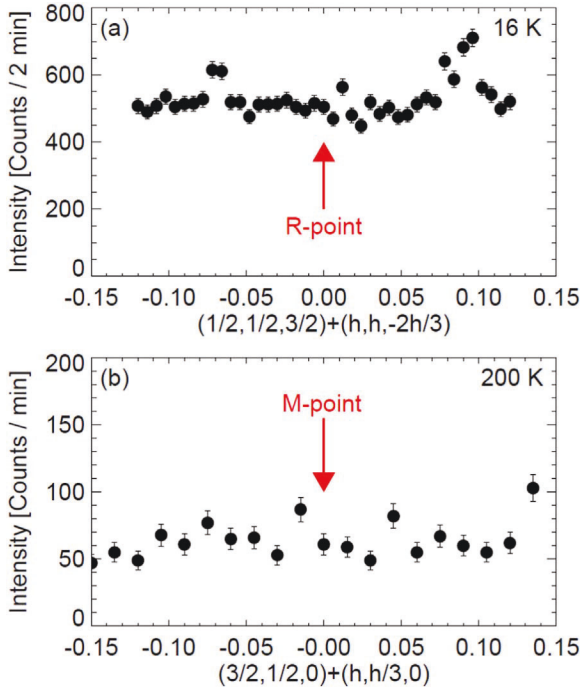

Fig. 4. Single crystal neutron diffraction measurements through an (a) R-point at (1/2, 1/2, 3/2) at 16 K and (b) an M-point (3/2, 1/2, 0) at 200 K. Both scans were performed in the direction transverse to the Bragg reflection.

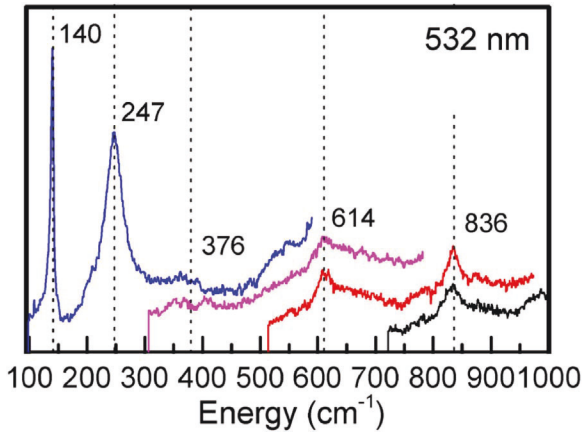

Fig. 5. Raman spectrum measured from a single crystal of $BaSnO_{3-\delta}$.

elastic constants under pressure and reported stability of the cubic phase under pressure (though the specific pressure range they investigated was unspecified).

3.6. Transverse acoustic phonons

We have measured the dispersion of the transverse acoustic phonon branches using the thermal neutron triple-axis with the three co-aligned crystals oriented in the (hk0) scattering plane. Because of the small combined mass of the three crystals, the measurements were performed at 700 K in order to enhance the scattering cross-section via increased phonon population. We have specifically measured the transverse branch in the (200) zone (T_1 Branch) for which the polarization is along [100] and propagation is along [010]. For the T_1 branch, the long-wavelength limit of dω/dk yields a sound velocity, v_{T1}, from which the elastic constant C_{44} can be determined [30] by $C_{44} = \rho v_{T1}^2$. We have also measured the transverse branch in the (220) zone (T_2 branch), for which the polarization is along [110] and propagation is along [1–10]. The sound velocity of the T_2 branch, v_{T2}, is related to C_{11} and C_{12} [30] via $\frac{1}{2}(C_{11} - C_{12}) = \rho v_{T2}^2$. We note that C_{11}, C_{12}, and C_{44} completely determine the elastic tensor of a cubic crystal [30]; unfortunately, we were unable to reliably measure the longitudinal phonon branches in either zone which prevented unique determination of C_{11} and C_{12}.

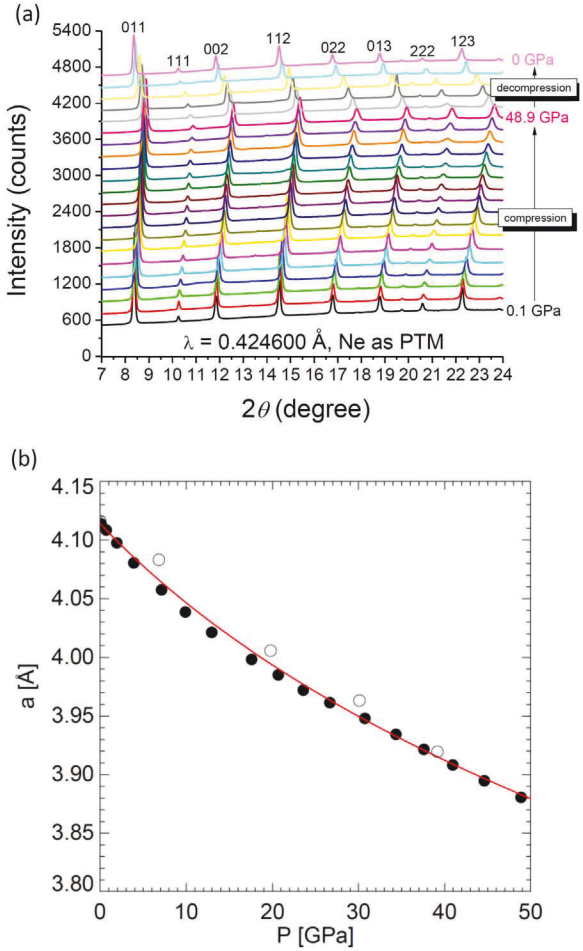

Fig. 6. (a) Pressure dependence of powder x-ray diffraction data. (b) Pressure dependence of the lattice parameter is shown in black circles. Solid data points represent the data on compression, whereas open points show data on decompression. The fit shown in the solid red line was derived from a fit to the third order Birch-Murnaghan equation describing the relationship between volume and pressure. (For interpretation of the references to color in this figure legend, the reader is referred to the web version of this article.)

Fig. 8 shows constant-$\boldsymbol{Q}$ measurements of the T_1 and T_2 branches (left and right columns respectively), from which the dispersions of the two branches are apparent. Because we employed vertical beam focusing to enhance the intensity, we consider the longest wavelength measurements in each zone, i.e., $\boldsymbol{Q}$ = (2.1,0,0) and $\boldsymbol{Q}$ = (2.07,1.93,0), unreliable for determining the sound velocities, as they may be unduly influenced by out-of-plane scattering. We have therefore estimated the sound velocities from the measurements at $\boldsymbol{Q}$ = (2.2,0,0) and $\boldsymbol{Q}$ = (2.14,1.86,0), finding v_{T1} = 3.64 km/s and v_{T2} = 3.94 km/s. This leads to estimates of $C_{44} = 9.48 \times 10^{10}$ Nm^{-2} and $(C_{11}\text{-}\ C_{12}) = 2.23 \times 10^{11}$ Nm^{-2}. Bouhemadou *et al.* previously calculated v_{T1} and v_{T2} via DFT. They determined v_{T1} as 3.51 and 3.82 km/s for GGA and LDA, respectively, and v_{T2} as 3.98 and 4.19 km/s [26]. Using ceramics, Maekawa *et al.* measured a shear wave velocity of 3.82 km/s via an ultrasonic pulse-echo method at room temperature [25]. Our estimates of the transverse sound velocities via phonon dispersion are thus in relatively good agreement with this prior work.

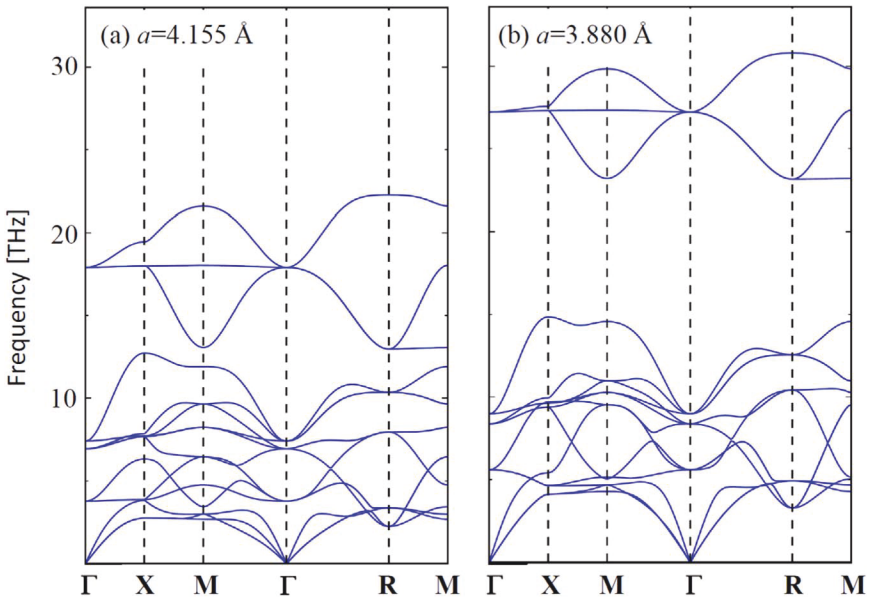

Fig. 7. Phonon dispersion calculations for (a) ambient pressure and (b) P~50 GPa. The lattice parameters of each cubic structure are denoted in (a) and (b).

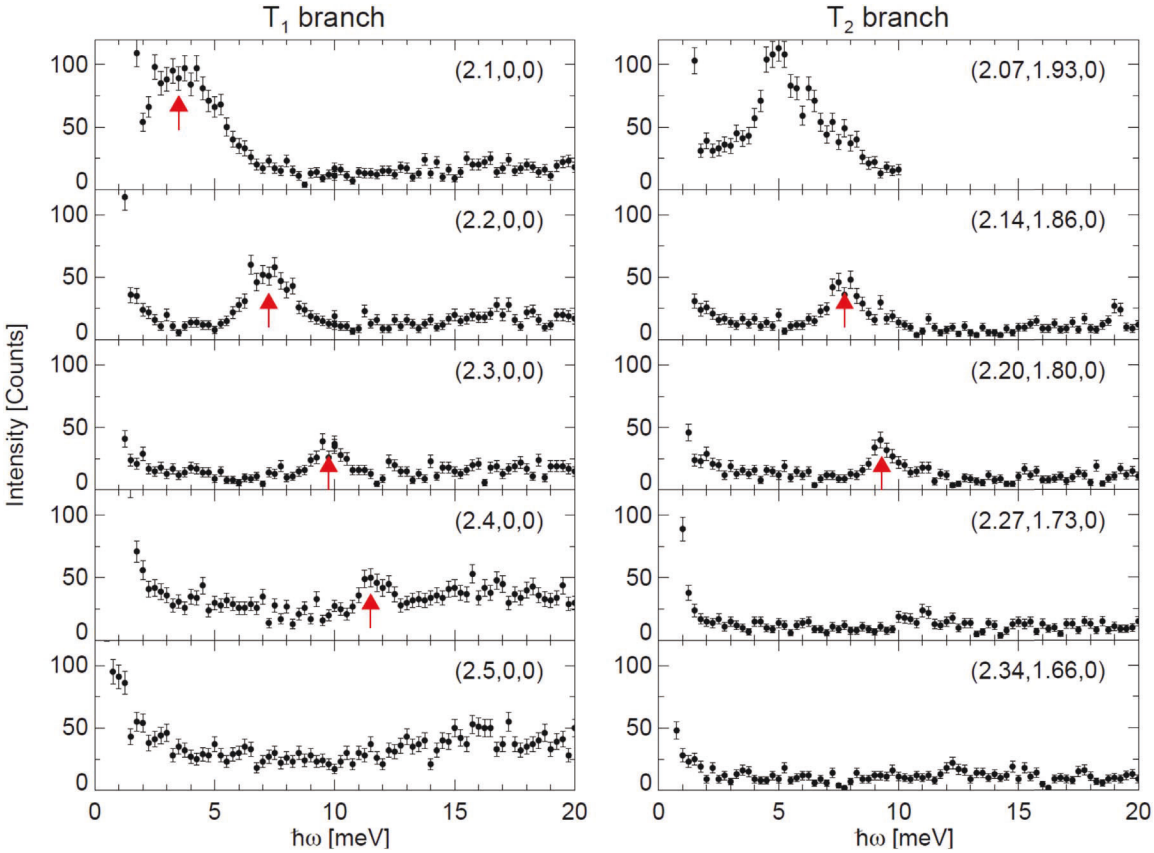

Fig. 8. Constant-**Q** measurements of the T_1 and T_2 phonon branches at 700 K. The arrows mark the transverse acoustic phonon peaks.

4. Conclusions

$BaSnO_3$ possesses long-range and short-range cubic symmetry as demonstrated by a wide variety of techniques employed in this work. We have performed diffraction measurements up to significantly higher pressures than had previously been reported and found that the cubic symmetry is remarkably stable under pressure. This stability suggests that $BaSnO_3$ possesses a large degree of flexibility in accommodating epitaxial growth on substrates with significantly smaller lattice constants, suggesting that such an approach could be used to investigate effects of strain on properties such as bandgaps, carrier concentrations, and electron mobilities, for instance.

Acknowledgments

This work was supported by the U.S. Department of Energy, Office of Science, Basic Energy Sciences, Materials Science and Engineering Division. We acknowledge the support of the National Institute of Standards and Technology, U.S. Department of Commerce, in providing the neutron research facilities used in this work. Use of the Advanced Photon Source at Argonne National Laboratory was supported by the U.S. Department of Energy, Office of Science, Office of Basic Energy Sciences, under Contract No. DE-AC02-06CH11357. ChemMatCARS Sector 15 is principally supported by the Divisions of Chemistry (CHE) and Materials Research (DMR), National Science Foundation, under grant number NSF/CHE-1346572. The NOMAD instrument at ORNL's SNS is sponsored by the DOE, SC, BES, Scientific User Facilities Division. The high pressure experiments were financially supported by the National Nature Science Foundation of China under Contract Nos. U1530402, 11374137, and 11525417. Y.G. and S.L.C. were supported by the National Science Foundation under Grant no. NSF DMR 1464090.

References

[1] O.I. Prokopalo, E.G. Fesenko, M.A. Malitskaya, Y.M. Popov, V.G. Smotrakov, Ferroelectrics 18 (1978) 99.
[2] G. Larramona, C. Gutierrez, I. Pereira, M.R. Nunes, F.M.A. da Costa, J. Chem. Soc. Faraday Trans. 1 (85) (1989) 907.
[3] H. Mizoguchi, H.W. Eng, P.M. Woodward, Inorg. Chem. 43 (2004) 1667.
[4] H.F. Wang, Q.Z. Liu, F. Chen, G.Y. Gao, W. Wu, X.H. Chen, J. Appl. Phys. 101 (2007) 106105.
[5] X. Luo, Y.S. Oh, A. Sirenko, P. Gao, T.A. Tyson, K. Char, S.-W. Cheong, Appl. Phys. Lett. 100 (2012) 172112.
[6] H.J. Kim, U. Kim, T.H. Kim, J. Kim, H.M. Kim, B.-G. Jeon, W.-J. Lee, H.S. Mun, K.T. Hong, J. Yu, K. Char, K.H. Kim, Phys. Rev. B 86 (2012) 165205.
[7] H.J. Kim, U. Kim, H.M. Kim, T.H. Kim, H.S. Mun, B.-G. Jeon, K.T. Hong, W.-J. Lee, C. Ju, K.H. Kim, K. Char, Appl. Phys. Express 5 (2012) 061102.
[8] W.-J. Lee, H.J. Kim, E. Sohn, T.H. Kim, J.-Y. Park, W. Park, H. Jeong, T. Lee, J.H. Kim, K.-Y. Choi, K.H. Kim, Appl. Phys. Lett. 108 (2016) 082105.
[9] S. Raghavan, T. Schumann, H. Kim, J.Y. Zhang, T.A. Cain, S. Stemmer, APL Mater. 4 (2016) 016106.
[10] H.J. Kim, T.H. Kim, W.-J. Lee, Y. Chai, J.W. Kim, Y.J. Jwa, S. Chung, S.J. Kim, E. Sohn, S.M. Lee, K.-Y. Choi, K.H. Kim, Thermochimica Acta 585 (2014) 16.
[11] K. Ganguly, P. Ambwani, P. Xu, J.S. Jeong, K.A. Mkhoyan, C. Leighton, B. Jalan, APL Mater. 3 (2015) 062509.
[12] H.-R. Liu, J.-H. Yang, H.J. Xiang, X.G. Gong, S.-H. Wei, Appl. Phys. Lett. 102 (2013) 112109.
[13] A.M. Glazer, Acta Cryst. B 28 (1972) 3384.
[14] T.N. Stanislavchuk, A.A. Sirenko, A.P. Litvinchuk, X. Luo, S.-W. Cheong, J. Appl. Phys. 112 (2012) 044108.
[15] J. Neuefeind, M. Feygenson, J. Carruth, R. Hoffmann, K.K. Chipley, Nuclear Instruments and Methods in Physics Research B 287 (2012) 68.
[16] A.C. Larson, R.B. Von Dreele, Los Alamos National Laboratory Report LAUR 86–748 (2004).
[17] B.H. Toby, J. Appl. Cryst. 34 (2001) 210.
[18] C.L. Farrow, P. Juhas, J.W. Liu, D. Bryndin, E.S. Bozin, J. Bloch, Th. Proffen, S.J.L. Billinge, J. Phys. Condens. Matter 19 (2007) 335219.
[19] T. Egami, S. Billinge, Underneath the Bragg Peaks: Structural Analysis of Complex Materials, Pergamon Press, Oxford, 2003.
[20] Th. Proffen, S.J.L. Billinge, T. Egami, D. Louca, Z. Kristallogr. 218 (2003) 132.
[21] M. Guennou, P. Bouvier, J. Kreisel, D. Machon, Phys. Rev. B 81 (2010) 054115.
[22] F. Birch, Phys. Rev. 71 (1947) 809.
[23] I. Errea, M. Calandra, C.J. Pickard, J.R. Nelson, R.J. Needs, Y. Li, H. Liu, Y. Zhang, Y. Ma, F. Mauri, Nature 532 (2016) 81.
[24] G.N. Stepanov, Phys. Solid State 56 (2014) 1561.
[25] T. Maekawa, K. Kurosaki, S. Yamanaka, J. Alloy. Compd. 416 (2006) 214.
[26] A. Bouhemadou, K. Haddadi, Solid State Sci. 12 (2010) 630.
[27] J. Heyd, G.E. Scuseria, M. Ernzerhof, J. Chem. Phys. 118 (2003) 8207.
[28] G. Kresse, J. Hafner, Phys. Rev. B 47 (1993) 558.
[29] A. Togo, I. Tanaka, Scripta Materialia 108 (2015) 1.
[30] Y. Noda, Y. Yamada, S.M. Shapiro, Phys. Rev. B 40 (1989) 5995.